

Consistent picture of electronic Raman scattering and infrared conductivity in the cuprates

T. P. Devereaux, Arno P. Kampf

Angaben zur Veröffentlichung / Publication details:

Devereaux, T. P., and Arno P. Kampf. 2000. "Consistent picture of electronic Raman scattering and infrared conductivity in the cuprates." *Physical Review B* 61 (2): 1490-94. <https://doi.org/10.1103/PhysRevB.61.1490>.

Nutzungsbedingungen / Terms of use:

licgercopyright

Dieses Dokument wird unter folgenden Bedingungen zur Verfügung gestellt: / This document is made available under the following conditions:

Deutsches Urheberrecht

Weitere Informationen finden Sie unter: / For more information see:

<https://www.uni-augsburg.de/de/organisation/bibliothek/publizieren-zitieren-archivieren/publizieren>



Consistent picture of electronic Raman scattering and infrared conductivity in the cuprates

T. P. Devereaux*

Department of Physics, The George Washington University, Washington, DC 20052

A. P. Kampf

Theoretische Physik III, Elektronische Korrelationen und Magnetismus, Institut für Physik, Universität Augsburg, D-86135 Augsburg, Germany

(Received 14 April 1999; revised manuscript received 6 October 1999)

Calculations are presented for electronic Raman scattering and infrared conductivity in a $d_{x^2-y^2}$ superconductor including the effects of elastic scattering via anisotropic impurities and inelastic spin-fluctuation scattering. A consistent description of experiments on optimally doped Bi-2212 is made possible by considering the effects of correlations on both inelastic and elastic scattering.

Impurity effects in the cuprates have played a major role in clarifying the nature of unconventional superconductivity. Via the change in the density of states (DOS) near the Fermi level, crossover behavior of low-temperature transport and thermodynamics quantities could be explored as a testing ground for unconventional pairing.¹ Examples include the T to T^2 crossover in the low-temperature magnetic penetration depth $\lambda(T)$, T^3 to T crossover in the NMR rate, and the ω^3 to ω crossover in the low-frequency B_{1g} Raman response. Simple theories based on nearly resonant scattering in the impurity T -matrix approximation (“dirty” d wave) have accounted for these behaviors seen in materials of various quality and impurity dopings.

However, several inconsistencies arise when attempting to put together a complete picture. First, the magnitude of the impurity scattering needed to fit $\lambda(T)$ and the extrapolated $T=0$ resistivity are generally much smaller than those needed to fit the measured frequency dependence of the infrared conductivity (IR) and the Raman response. In particular, the impurity scattering rate $1/\tau_{imp} = 2\Gamma$ needed to fit the IR on high-quality Y-123 was 100 times larger than that needed to fit microwave measurements,² while values of Γ/Δ_0 ranging up to 0.5 were needed to interpret the Raman data taken on Bi-2201,³ and some samples of Tl-2201 (Ref. 4) and Hg-1223.⁵ Second, the “universal” dc conductivity $\sigma(\omega \rightarrow 0, T=0) = (e^2/2\pi\hbar)\xi/a$ (Ref. 6) has not been convincingly observed and the low-temperature variation of the conductivity $\delta\sigma(T)$ changes slower than T^2 .⁷ Third, the transition temperature T_c is only moderately reduced by planar impurities compared to Abrikosov-Gorkov theory⁸ (by about a factor of 2–3). Lastly, the residual resistivity obtained for Zn-doped Y-123 suggests that a strong contribution is present in d -wave scattering channels.⁹

These inconsistencies reveal that the usual treatment of pointlike s -wave impurities in a T -matrix approach may be too naive and neglects electronic correlations. Experimental evidence from transport measurements in Zn-doped Y-Ba-Cu-O have revealed that the a single impurity embedded in the CuO_2 plane disturbs the local environment and yields an effective scattering cross-section diameter of Zn^{2+} of 4.2 Å,¹⁰ and is thus extended. Theoretical studies have shown that static vacancies in a Heisenberg antiferromagnet en-

hance the staggered magnetic moment within a few lattice spacings around the vacancy,¹¹ while studies of models with only short-range antiferromagnetic (AF) correlations have shown that correlations dynamically generate finite-range impurity potentials from single-site impurities.¹²

In this paper we explore the role extended impurities have on transport properties in an attempt to resolve the above-mentioned discrepancies. In particular, we reexamine the IR and the electronic Raman response of Bi-2212 including the effects of electronic correlations on both inelastic and elastic scattering potentials, and compare our results with the extrapolated $T=0$ normal-state resistivity and the crossover temperature for $\lambda(T)$. We find that a consistent picture emerges when we include the extended range of impurity scattering as well as AF spin fluctuations.

Currently, knowledge of a T -matrix formulation for disorder in correlated systems is limited and generally approximate methods have been used.¹³ Formally, one would need to include not only bare impurity and interaction self-energies responsible for elastic and inelastic scattering, respectively, but also one must include terms in which elastic and inelastic potentials mix. In this way, a purely static bare impurity interaction changes in nature (can become dynamic) due to the inclusion of many-body effects. Ziegler *et al.*¹³ discussed how a pointlike s -wave bare impurity potential can become extended due to the background of the correlated host. One can then proceed to calculate the T matrix by using a *renormalized* Hamiltonian which describes the impurity potential in the correlated host.

Our starting point is the model Hamiltonian considered in Ref. 14, which represents the effects of impurities in a metal with short-range AF order on a square lattice:

$$H_i = \sum_{\{l, \sigma, \delta\}} \left[\frac{V_0}{4} n_{l, \sigma} + t_l (c_{l, \sigma}^\dagger c_{l+\delta, \sigma} + \text{H.c.}) + V_1 n_{l+\delta, \sigma} \right].$$

The parameters V_0 and V_1 denote the on-site and extended impurity potentials, and t_l denotes the effect of impurities on the electron hopping to the impurity site. Focusing on a two-parameter model using the specific relation $V_1 = \alpha^2 V_0/4$ and $t_l = \alpha V_0/4$, an analytic solution for the single-impurity T ma-

trix was obtained. α is the control parameter which distinguishes between pointlike ($\alpha=0$) and extended ($\alpha\neq 0$) impurity potentials.

The algebraic solution for the impurity T matrix is presented in Ref. 14, where the reader is referred to for details. In essence, the extended structure of the impurity potential requires a 4×4 matrix formulation with respect to s , p , and d scattering channels expressed in terms of the \mathbf{k} -dependent basis functions of the square lattice. The impurity-averaged self-energy is determined via $\hat{\Sigma}_i^{imp}(\mathbf{k}, i\omega) = n_i \hat{T}_{\mathbf{k}, \mathbf{k}}(i\omega)$, with n_i the impurity concentration. The self-energy can be expanded in Pauli matrices $\hat{\Sigma}_i^{imp} = \sum_{i=0,3} \hat{\tau}_i \hat{\Sigma}_i^{imp}$, with the coefficients

$$\begin{aligned} \Sigma_0^{imp}(\mathbf{k}, i\omega) = & \frac{n_i V_0}{\delta^2 - \beta^2} \{ -(1 + \alpha \gamma_{\mathbf{k}})^2 (d_0 \beta + d_3 \delta) \\ & + (\alpha \gamma_{\mathbf{k}}^d)^2 (s_0 \beta - s_3 \delta) \} \\ & - \frac{n_i V_0 p_3 \alpha^2 ([\gamma_{\mathbf{k}}^{p1}]^2 + [\gamma_{\mathbf{k}}^{p2}]^2)}{p_0^2 - p_3^2 + a^{-2}}, \end{aligned} \quad (1)$$

$$\Sigma_1^{imp}(\mathbf{k}, i\omega) = \gamma_{\mathbf{k}}^d 2 \alpha n_i V_0 \left\{ \frac{(1 + \alpha \gamma_{\mathbf{k}}) a^+ \delta}{\delta^2 - \beta^2} + \frac{\alpha \gamma_{\mathbf{k}} a^-}{p_0^2 - p_3^2 + a^2} \right\},$$

$$\begin{aligned} \Sigma_3^{imp}(\mathbf{k}, i\omega) = & \frac{n_i V_0}{\delta^2 - \beta^2} \{ (1 + \alpha \gamma_{\mathbf{k}})^2 (d_0 \delta + d_3 \beta) \\ & + (\alpha \gamma_{\mathbf{k}}^d)^2 (s_0 \delta - s_3 \beta) \} \\ & + \frac{n_i V_0 p_0 \alpha^2 ([\gamma_{\mathbf{k}}^{p1}]^2 + [\gamma_{\mathbf{k}}^{p2}]^2)}{p_0^2 - p_3^2 + a^{-2}}, \end{aligned}$$

and $\Sigma_2^{imp}(\mathbf{k}, i\omega) = 0$. Here $s_{0,3}$, $d_{0,3}$, $p_{0,3}$, δ , β , and a^\pm are constants¹⁵ given by Eqs. (8)–(11) of Ref. 14. The \mathbf{k} -dependent basis functions for a square lattice are $\gamma_{\mathbf{k}}, \gamma_{\mathbf{k}}^d = [\cos(k_x a) \pm \cos(k_y a)]/2$, and $\gamma_{\mathbf{k}}^{p1}, \gamma_{\mathbf{k}}^{p2} = [\sin(k_x a) \pm \sin(k_y a)]/2$. In the limit of $\alpha \rightarrow 0$, the T matrix becomes momentum independent and recovers the well-known results.¹⁶

In the self-consistent T -matrix approximation, the noninteracting Green's function is used to calculate the self-energy and then the new Green's function is put back into the self-energy calculation. The process is iterated until convergence is realized, which occurs typically after only a few iterations. We assume a strong on-site impurity interaction $V_0 = 8t$, take $\epsilon_{\mathbf{k}} = -2t[\cos(k_x a) + \cos(k_y a)] + 4t' \cos(k_x a) \cos(k_y a) - \mu$, $\Delta_{\mathbf{k}}(T) = \Delta_0(T)[\cos(k_x a) - \cos(k_y a)]/2$, a weak-coupling form for $\Delta_0(T)$, and choose $\Delta_0(T=0) = 4T_c = 0.4t$. Here and throughout, lattice sizes of 32×32 up to 256×256 and typically over 1000 frequencies were used. Our results showed little size effects above the 128×128 mesh. The chemical potential μ was adjusted so that the filling $\langle n \rangle = 0.825$.

In the absence of vertex corrections, the homogeneous Raman response and the real part of the conductivity are

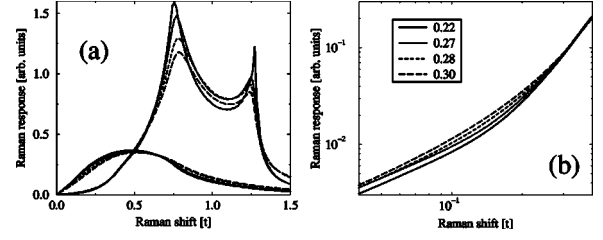


FIG. 1. (a) B_{1g} (upper set) and B_{2g} (lower) Raman response for $T = 0.2T_c$, $\bar{U} = 0$, and 1% impurities. Here and in (b) the solid (dotted, dashed, long-dashed) line corresponds to $\alpha = 0(0.5, 0.75, 1)$. (b) Log-log plot of the low-frequency B_{1g} Raman response determining the crossover frequency ω^* . The legend gives the values of ω^*/t .

$$\begin{aligned} \left. \begin{aligned} \chi''_{\gamma, \gamma}(\mathbf{q} = \mathbf{0}, \Omega) \\ \Omega \sigma'_{xx}(\mathbf{q} = \mathbf{0}, \Omega) \end{aligned} \right\} = & \sum_{\mathbf{k}} \frac{\gamma_{\mathbf{k}}^2}{j_{\mathbf{k}}^2} \int \frac{d\omega}{N\pi} [f(\omega) - f(\omega + \Omega)] \\ & \times \text{Tr} \left\{ \begin{aligned} \hat{\tau}_3 \hat{G}''(\mathbf{k}, \omega) \hat{\tau}_3 \hat{G}''(\mathbf{k}, \omega + \Omega) \\ \hat{\tau}_0 \hat{\tau}_0 \end{aligned} \right\}, \end{aligned} \quad (2)$$

where f is the Fermi function and the current vertex $j_{\mathbf{k}}^x = e \partial \epsilon_{\mathbf{k}} / \partial k_x = 2te a \sin(k_x a) [1 - 2t'/t \cos(k_y a)]$. The Raman response can be classified according to elements of the D^{4h} group:

$$\gamma_{\mathbf{k}}(\omega_I, \omega_S) = \begin{cases} b_{\omega_I, \omega_S} [\cos(k_x a) - \cos(k_y a)]/4, & B_{1g}, \\ b'_{\omega_I, \omega_S} \sin(k_x a) \sin(k_y a), & B_{2g}, \\ a_{\omega_I, \omega_S} [\cos(k_x a) + \cos(k_y a)]/4, & A_{1g}. \end{cases} \quad (3)$$

If the light scattering is nonresonant, the frequency dependence of the momentum-independent prefactors b , b' , and a can be safely neglected, and we can adjust these prefactors to account for overall intensity. It can be seen from the \mathbf{k} dependence of the vertices that the B_{1g} response probes qp dynamics around the Brillouin zone (BZ) axes, B_{2g} probes the diagonals, and A_{1g} is more of an average around the BZ and involves pure density fluctuations and backflow.¹⁷ Higher-order terms of increasingly more anisotropic basis functions could be considered but do not lead to appreciable differences except for the A_{1g} response (see Ref. 18 for details). From here on we only consider the B_{1g} and B_{2g} channels.

Results for the B_{1g} and B_{2g} response are plotted in Fig. 1(a) for different values of α . As seen in our previous studies of the DOS,¹⁴ turning on α even slightly leads to an effective increase in the strength of the impurity potential. The increased impurity resonance at the Fermi level is manifest in the increasingly smeared spectra as well as the value of ω^* , defined as the frequency where the cubic frequency dependence becomes subdominant,¹⁹ as shown in Fig. 1(b). Since $\alpha = 0.5$ corresponds to a nearest-neighbor impurity potential $V_1 = V_0/16$, the presence of even a 6% nearest-neighbor potential leads to a 23% increase in ω^* . Therefore a much smaller concentration of extended impurities is needed to have the same effect as isotropic impurity scattering. The B_{2g} channel is only slightly affected by α .

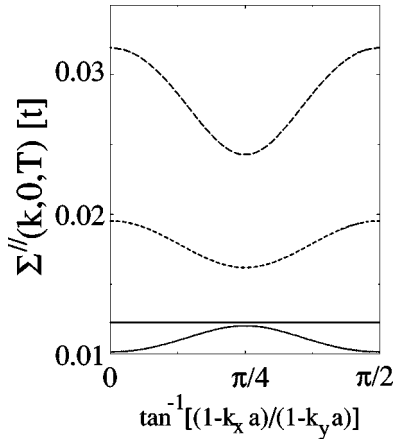


FIG. 2. The impurity scattering rate for momenta along the Fermi surface for $\alpha=0, 0.24, 0.48,$ and 0.72 (solid, dotted, dashed, long-dashed lines, respectively).

This is in accord with the impurity scattering being largest near the BZ axes in our model and only minorly dependent on α near the BZ diagonals. This is seen in Fig. 2, which plots the normal-state $T=0$ impurity scattering rate around the Fermi surface for different α . Increasing α from zero first decreases then increases the scattering rate near the BZ axes while only mildly affecting the rate along the BZ diagonals. Therefore we would expect the B_{1g} channel to be more sensitive than B_{2g} to the growth of scattering for increased α .

As an important consequence, the IR (which has similar weighting to B_{2g}) does not pick up regions where the scattering changes rapidly and is governed by small scattering along the BZ diagonals. The IR in the superconducting state is shown in Fig. 3 for different values of α at a fixed impurity concentration. The IR does not appreciably change for α up to 0.5. For larger α spectral weight is shifted away from low frequencies as the scattering rate increases over the entire BZ,²⁰ and a stronger shoulder near Δ_{max} develops.

We now consider inelastic scattering in order to address the intensity observed at high frequencies. The origin of the flat background in IR and Raman at high frequencies has attracted a great deal of attention involving both Fermi-

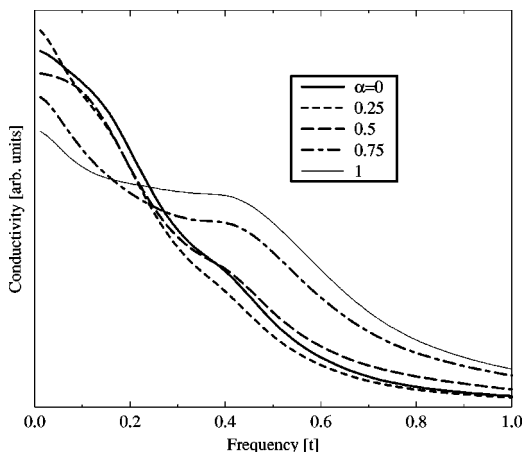


FIG. 3. The calculated IR at $T=0.2T_c$, $U=0$, and 2% impurities for $\alpha=0, 0.25, 0.5, 0.75,$ and 1 (solid, dashed, long-dashed, dash-dotted lines, and thin solid lines, respectively).

liquid- and non-Fermi-liquid-based theories. A correct approach would account not only for the featureless continuum but would be able to describe the polarization dependence of the Raman cross section and the differences between IR and Raman. Raman has shown strong evidence of two-magnon features in the insulating as well as superconducting state, implying the role of spin fluctuations as a source for inelastic scattering.²¹ The way in which spin fluctuations are included in calculating dynamic quantities has also attracted a large amount of attention. The main problem has been the degree in which strong local electron correlations are included and represented. Effective Hamiltonian²² approaches based on Bragg-like scattering of quasiparticles for momentum $\mathbf{Q}=(\pi, \pi)$ have been successfully employed to calculate various dynamic correlation functions, including IR (Ref. 23) and Raman.²⁴ However, to a certain extent these approaches have their limitation as they do not adequately capture the strong multimagnon scattering process required to approach the insulating phase from the metallic side.²⁵

Since here we are interested in only the low-frequency behavior of the IR and Raman response, the details of the dynamic scattering are not crucial in that they only affect the response functions at larger frequencies. Therefore we take a simple route and include spin fluctuations in the random-phase approximation (RPA),

$$V(\mathbf{q}, i\Omega) = \frac{3}{2} \frac{\bar{U}^2 \chi_0(\mathbf{q}, i\Omega)}{1 - \bar{U} \chi_0(\mathbf{q}, i\Omega)}, \quad (4)$$

where \bar{U} is a phenomenological parameter (we choose $\bar{U}=2t$). $\chi_0(\mathbf{q}, i\Omega)$ is the noninteracting spin susceptibility,

$$\chi_0(\mathbf{q}, i\Omega) = \sum_{\mathbf{k}} \left\{ \frac{a_{\mathbf{k}, \mathbf{k}+\mathbf{q}}^+}{2N} \frac{f(E_{\mathbf{k}+\mathbf{q}}) - f(E_{\mathbf{k}})}{i\Omega - (E_{\mathbf{k}+\mathbf{q}} - E_{\mathbf{k}})} + \frac{a_{\mathbf{k}, \mathbf{k}+\mathbf{q}}^-}{4N} \left[\frac{1 - f(E_{\mathbf{k}+\mathbf{q}}) - f(E_{\mathbf{k}})}{i\Omega + E_{\mathbf{k}+\mathbf{q}} + E_{\mathbf{k}}} - \frac{1 - f(E_{\mathbf{k}+\mathbf{q}}) - f(E_{\mathbf{k}})}{i\Omega - E_{\mathbf{k}+\mathbf{q}} - E_{\mathbf{k}}} \right] \right\}. \quad (5)$$

Here $E_{\mathbf{k}}^2 = \epsilon_{\mathbf{k}}^2 + \Delta_{\mathbf{k}}^2$ and the coherence factors are $a_{\mathbf{k}, \mathbf{k}+\mathbf{q}}^{\pm} = 1 \pm (\epsilon_{\mathbf{k}+\mathbf{q}} \epsilon_{\mathbf{k}} + \Delta_{\mathbf{k}} \Delta_{\mathbf{k}+\mathbf{q}}) / E_{\mathbf{k}+\mathbf{q}} E_{\mathbf{k}}$. This yields a self-energy

$$\begin{aligned} \hat{\Sigma}^{\bar{U}}(\mathbf{k}, i\omega) = & - \int \frac{dx}{\pi N} \sum_{\mathbf{q}} V''(\mathbf{q}, x) \frac{1}{2E_{\mathbf{k}-\mathbf{q}}} \\ & \times \left[\frac{E_{\mathbf{k}-\mathbf{q}} \hat{\tau}_0 + \epsilon_{\mathbf{k}-\mathbf{q}} \hat{\tau}_3 + \Delta_{\mathbf{k}-\mathbf{q}} \hat{\tau}_1}{E_{\mathbf{k}-\mathbf{q}} + x - i\omega} \right. \\ & \times [n(x) + f(-E_{\mathbf{k}-\mathbf{q}})] \\ & \left. - \frac{-E_{\mathbf{k}-\mathbf{q}} \hat{\tau}_0 + \epsilon_{\mathbf{k}-\mathbf{q}} \hat{\tau}_3 + \Delta_{\mathbf{k}-\mathbf{q}} \hat{\tau}_1}{-E_{\mathbf{k}-\mathbf{q}} + x - i\omega} \right. \\ & \left. \times [n(x) + f(E_{\mathbf{k}-\mathbf{q}})] \right]. \quad (6) \end{aligned}$$

The convolution of momentum sums in Eq. (6) is solved numerically via fast Fourier transform, where we keep the full \mathbf{k} dependence and the real and imaginary parts of the self-energy. We found that neglecting the real parts of the

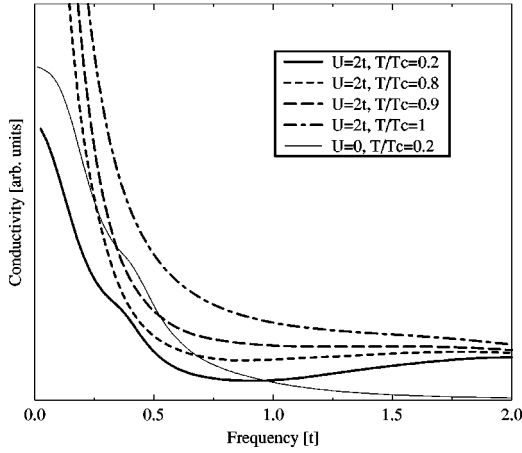


FIG. 4. The IR conductivity for $T=0.2, 0.8, 0.9$, and T_c (solid, dashed, long-dashed, dash-dotted lines, respectively) for 2% impurities and $\alpha=0.5$ and $U=2t$. The thin solid line is for $U=0, T=0.2T_c$ for comparison.

self-energy and/or restricting momentum sums around the Fermi surface (FS) leads to a substantially smaller conductivity and misses a renormalization of the conductivity peak to frequencies slightly away from 4Δ in the superconducting state.² Combining both $\Sigma^{imp, U}$, the results for the IR and the Raman response for the B_{1g} and B_{2g} channels are summarized in Figs. 4 and 5. For both quantities the spin fluctuations yield a flat continuum at high frequencies in common with experiments and various different theories which yield a linear frequency dependence of the imaginary part of the self-energy. The temperature dependence there is minimal and all the spectra converge to similar values by roughly $\Omega \sim 2t$. As the temperature is lowered, the low-frequency IR falls in magnitude and develops a shoulder at $\sim \Delta_{max}$ and a weak peak at $\sim 4\Delta_{max}$, while the spectral weights in the B_{1g} and B_{2g} channels reorganize from low frequencies to higher frequencies at $\sim 2\Delta_{max}$ and $0.65\Delta_{max}$, respectively. Strong peaks associated with pair breaking and the van Hove structure ($\sim t$) appear in the B_{1g} channel and become less pronounced as the temperature is increased due to the growth of

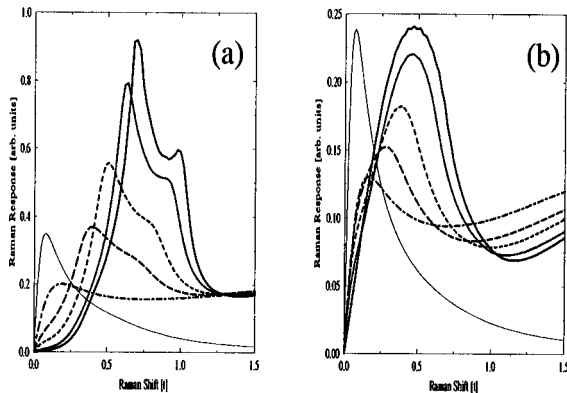


FIG. 5. Raman response for the B_{1g} (a) and B_{2g} (b) channel for $\bar{U}=2t, V_0=8t$, 2% impurities, and $\alpha=0.5$ for $T/T_c=0.2, 0.6, 0.8, 0.9, 1$ plotted as the thick solid, dotted, dashed, long-dashed, and dotted-dashed lines. The thin solid line shows the response at $T=T_c$ for $\bar{U}=0$ for comparison.

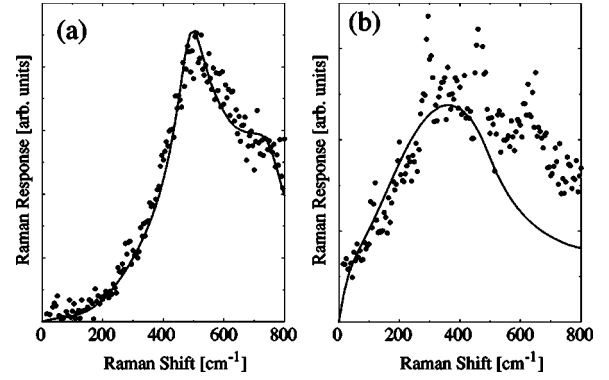


FIG. 6. Fits to the B_{1g} (a) and B_{2g} (b) low-temperature spectra on Bi-2212 ($T_c=86$ K) taken by Einzel and Hackl in Ref. 3.

spin fluctuation scattering. We note that at present there is no experimental indication of a peak in the B_{1g} which could be associated with a van Hove feature.³ In our calculations further smearing of the van Hove peak is expected if dispersion is added in the c direction or if stronger interactions are used which produce larger inelastic scattering at large frequencies. Moreover, a more correct multimagnon approach would also wash out structure at higher frequencies.

Fits to the Raman spectra measured in the superconducting state at $T=0.5T_c$ of an as-grown sample of Bi-2212 are presented in Fig. 6, while fits to the IR in both the normal and superconducting state on a similar sample with a slightly higher T_c as taken by Wang *et al.*²⁶ are shown in Fig. 7. Here we have taken the parameters used in Fig. 5 and have adjusted the prefactors $b/b'=1.46$ to account for the relative Raman intensities. For the IR, we use the c -axis lattice spacing of 30 Å for Bi-2212 containing two CuO_2 bilayers to convert the two-dimensional IR to three-dimensional. We find that theory underestimates the IR scale by a factor of only 1.5 (the fits in Fig. 7 are scaled by this factor). We used slightly different values of t for Raman (81 meV) than IR (69

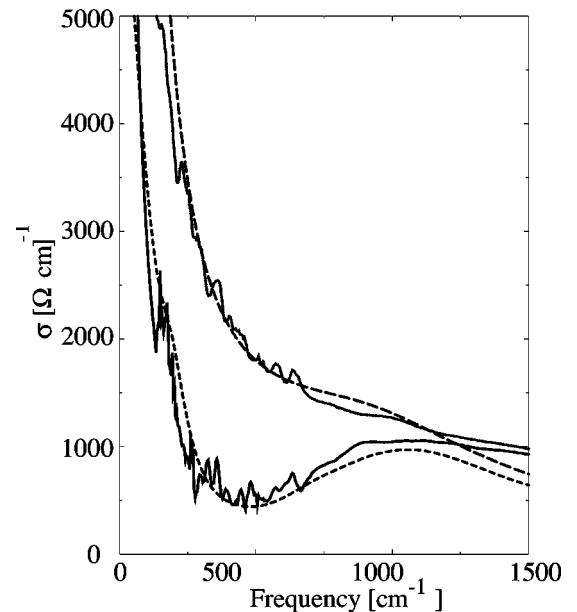


FIG. 7. Fits to the normal and superconducting IR on Bi-2212 ($T_c=93$ K) taken by Wang *et al.* (Ref. 26).

meV), but equally good fits are obtained if we used different values for Δ . The results agree exceptionally well with the measured spectra especially at low frequencies where the effects of impurities are dominant. The agreement lessens to only a qualitative level for $\Omega > 1000 \text{ cm}^{-1}$ due to the small degree of spin fluctuations included (in RPA) and points to an inadequate description of the normal state.

Finally, we consider how the fitting parameters compare to transport data. Assuming a Drude model for $\rho(T=0)$ ($\approx 10 \mu\Omega \text{ cm}$) and a plasma frequency of 1.2 eV (Ref. 27) implies a scattering rate $1/\tau_{imp} = 15 \text{ cm}^{-1}$, while the penetration depth T to T^2 crossover²⁸ measured in the same sample²⁹ as the Raman data gives 12 cm^{-1} . Previous Raman fits using isotropic impurity scattering only and a Fermi surface restricted approach required $1/\tau_{imp} = 2\Gamma = 72 \text{ cm}^{-1}$.¹⁹ Our calculation for $\alpha = 0.5$ yields $1/\tau_{imp}^{ave} = 23$ and 20 cm^{-1} for the FS averaged impurity scattering rate for the $t = 81$ and 69 meV , respectively. Given the uncertainty in estimating

$\rho(T=0)$ and ω_{pl} , this is in favorable agreement with existing measurements.

In summary we have shown how the inclusion of electron correlations in both inelastic and elastic scattering potentials leads to a consistent description of the channel-dependent Raman and IR response and lead to better fits than previously achieved. The overall intensity of the IR can be accounted for and the effect of extended impurities on the low-frequency behavior of the Raman response can resolve the discrepancy between large impurity scattering rates needed previously for IR and Raman fits and the small rates needed for transport.

Acknowledgment (T.P.D.) is made to the Donors of the Petroleum Research Fund, administered by the American Chemical Society, for partial support of this research. We have benefited from discussions with J. C. Irwin and R. Hackl, and we thank R. Hackl and N. L. Wang for sharing the data presented in Figs. 6 and 7, respectively.

*Present address: Department of Physics, University of Waterloo, Waterloo, Canada, ON N2L 3G1.

¹J. Annett, N. Goldenfeld, and A. J. Leggett, in *Physical Properties of High Temperature Superconductors*, edited by D. M. Ginsberg (World Scientific, Singapore, 1996), Vol. 5.

²S. M. Quinlan, P. J. Hirschfeld, and D. J. Scalapino, *Phys. Rev. B* **53**, 8575 (1996).

³D. Einzel and R. Hackl, *J. Raman Spectrosc.* **27**, 307 (1996).

⁴R. Nemetschek, O. V. Misochko, B. Stadlober, and R. Hackl, *Phys. Rev. B* **47**, 3450 (1993).

⁵A. Sacuto, R. Combescot, N. Bontemps, C. A. Müller, V. Viallet, and D. Colson, *Phys. Rev. B* **58**, 11 721 (1998).

⁶P. A. Lee, *Phys. Rev. Lett.* **71**, 1887 (1993).

⁷S. Hensen, G. Müller, C. T. Rieck, and K. Scharnberg, *Phys. Rev. B* **56**, 6237 (1997); A. Hosseini, R. Harris, S. Kamal, P. Dosanjh, J. Preston, R. Liang, W. N. Hardy, and D. A. Bonn, *ibid.* **60**, 1349 (1999).

⁸R. J. Radtke, K. Levin, H.-B. Schüttler, and M. R. Norman, *Phys. Rev. B* **48**, 653 (1993); L. P. Gor'kov and P. A. Kalugin, *Pis'ma Zh. Éksp. Teor. Fiz.* **41**, 208 (1985) [*JETP Lett.* **41**, 253 (1985)]; P. Fulde, J. Keller, and G. Zwicknagl, in *Solid State Physics*, edited by F. Seitz, D. Turnbull, and H. Ehrenreich (Academic Press, New York, 1988), Vol. 41.

⁹D. J. C. Walker, A. P. Mackenzie, and J. R. Cooper, *Phys. Rev. B* **51**, 15 653 (1995).

¹⁰T. R. Chien, Z. Z. Wang, and N. P. Ong, *Phys. Rev. Lett.* **67**, 2088 (1991).

¹¹N. Bulut, D. Hone, D. J. Scalapino, and E. Y. Loh, *Phys. Rev. Lett.* **62**, 2192 (1989).

¹²D. Poilblanc, D. J. Scalapino, and W. Hanke, *Phys. Rev. Lett.* **72**, 884 (1994); A. V. Balatsky, M. I. Salkola, and A. Rosengren, *Phys. Rev. B* **51**, 15 547 (1995); T. Xiang and J. M. Wheatley, *ibid.* **51**, 11 721 (1995).

¹³W. Ziegler, D. Poilblanc, R. Preuss, W. Hanke, and D. J. Scalapino, *Phys. Rev. B* **53**, 8704 (1996).

¹⁴A. P. Kampf and T. P. Devereaux, *Phys. Rev. B* **56**, 2360 (1997).

¹⁵The constants s_i, d_i, p_i are the i th Pauli matrix prefactor for the

matrices $\hat{s}, \hat{d}, \hat{p}$ in Eq. (8) of Ref. 14, $a^\pm = a_2 \pm c_2$, with $a_2 = -(V_0/4N)\sum_{\mathbf{k}} 2\alpha\gamma_{\mathbf{k}}^d g_1$, $c_2 = -(V_0/4N)\sum_{\mathbf{k}} [2\alpha\gamma_{\mathbf{k}}^d + \alpha^2[\cos(2k_x a) + \cos(2k_y a)]/2] g_1$, and $\delta \pm \beta = (s_0 \pm s_3)(d_0 \mp d_3) + a^{\pm 2}$.

¹⁶P. J. Hirschfeld, P. Wölfle, and D. Einzel, *Phys. Rev. B* **37**, 83 (1988).

¹⁷Note that the term ‘‘screening’’ has been used to describe the backflow. However, the backflow is independent of the charge of the carriers and comes into play solely from the pair interactions responsible for superconductivity. It yields the well-known Anderson-Bogoliubov mode which restores gauge invariance. Details can be found in T. P. Devereaux and D. Einzel, *Phys. Rev. B* **51**, 16 336 (1995).

¹⁸T. P. Devereaux, A. Virosztek, and A. Zawadowski, *Phys. Rev. B* **54**, 12 523 (1996).

¹⁹T. P. Devereaux, *Phys. Rev. Lett.* **74**, 4313 (1995); T. P. Devereaux and A. P. Kampf, *Int. J. Mod. Phys. B* **11**, 2093 (1997).

²⁰Vertex corrections must be included for finite α . However, these corrections are proportional to α^2 and thus not important for small α .

²¹M. Rübhausen, O. A. Hammerstein, A. Bock, U. Merkt, C. T. Rieck, P. Guptasarma, D. G. Hinks, and M. V. Klein, *Phys. Rev. Lett.* **82**, 5349 (1999).

²²D. Pines, in *The Gap Symmetry and Fluctuations in High Temperature Superconductors*, edited by J. Bok and G. Deutscher (Plenum Press, New York, 1998), p. 111.

²³B. Stojković and D. Pines, *Phys. Rev. B* **56**, 11 931 (1997).

²⁴T. P. Devereaux and A. P. Kampf, *Phys. Rev. B* **59**, 6411 (1999).

²⁵J. R. Schrieffer, *J. Low Temp. Phys.* **99**, 397 (1995).

²⁶N. L. Wang, A. W. McConnell, B. P. Clayman, and G. D. Gu, *Phys. Rev. B* **59**, 576 (1999).

²⁷L. Forro, G. L. Carr, G. P. Williams, D. Mandrus, and L. Mihaly, *Phys. Rev. Lett.* **65**, 1941 (1990).

²⁸P. J. Hirschfeld and N. Goldenfeld, *Phys. Rev. B* **48**, 4219 (1993).

²⁹O. Waldmann, F. Steinmeyer, P. Müller, J. J. Neumeier, F. X. Régi, H. Savary, and J. Schneck, *Phys. Rev. B* **53**, 11 825 (1996).